Bulletin of the Seismological Society of America, Vol. 96, No. 6, pp. 2118–2130, December 2006, doi: 10.1785/0120060036

Prediction of Broadband Ground-Motion Time Histories: Hybrid Low/High-Frequency Method with Correlated Random Source Parameters

by Pengcheng Liu, Ralph J. Archuleta, and Stephen H. Hartzell

Abstract We present a new method for calculating broadband time histories of ground motion based on a hybrid low-frequency/high-frequency approach with correlated source parameters. Using a finite-difference method we calculate low-frequency synthetics ($< \sim 1$ Hz) in a 3D velocity structure. We also compute broadband synthetics in a 1D velocity model using a frequency-wavenumber method. The low frequencies from the 3D calculation are combined with the high frequencies from the 1D calculation by using matched filtering at a crossover frequency of 1 Hz. The source description, common to both the 1D and 3D synthetics, is based on correlated random distributions for the slip amplitude, rupture velocity, and rise time on the fault. This source description allows for the specification of source parameters independent of any *a priori* inversion results. In our broadband modeling we include correlation between slip amplitude, rupture velocity, and rise time, as suggested by dynamic fault modeling. The method of using correlated random source parameters is flexible and can be easily modified to adjust to our changing understanding of earthquake ruptures. A realistic attenuation model is common to both the 3D and 1D calculations that form the low- and high-frequency components of the broadband synthetics. The value of Q is a function of the local shear-wave velocity. To produce more accurate high-frequency amplitudes and durations, the 1D synthetics are corrected with a randomized, frequency-dependent radiation pattern. The 1D synthetics are further corrected for local site and nonlinear soil effects by using a 1D nonlinear propagation code and generic velocity structure appropriate for the site's National Earthquake Hazards Reduction Program (NEHRP) site classification. The entire procedure is validated by comparison with the 1994 Northridge, California, strong ground motion data set. The bias and error found here for response spectral acceleration are similar to the best results that have been published by others for the Northridge rupture.

Introduction

With increasing usage of nonlinear analysis techniques in the seismic design of structures, synthesizing time histories of ground motion becomes more important for the complete determination of structural response and damage estimation from future large earthquakes. Although we cannot know the exact time of the next damaging earthquake, geologists, seismologists, and geodesists have delineated faults that are capable of producing large-magnitude earthquakes in urban areas. For example, recent work by Shaw *et al.* (2002) has spotlighted the Puente Hills thrust fault system that underlies the Los Angeles metropolitan area. This system is capable of producing earthquakes from M_w 6.5 to 7.2 with serious consequences for the economy and humankind (Field *et al.*, 2005). To take full advantage of the database of likely scenario earthquakes, an accurate method of calculating expected ground motions is needed.

Within a few fault lengths and at frequencies of engineering interest (e.g., 0.1 to 20 Hz), ground-motion estimates strongly depend on fault geometry, detailed rupture processes, wave-propagation paths, and local site conditions. All of these characteristics are complicated, and an accurate description of most of them is not readily available. As a consequence we are forced to make many assumptions when constructing source models and generating Green's functions to estimate ground motions. Recently, in a systematic check of various methods Hartzell *et al.* (1999) compared 13 approaches by synthesizing 29 three-component records for the 1994 Northridge earthquake. These approaches used different assumptions to model the source process and/or the path effects. In general, most of these methods have numerous free parameters, and the misfit of almost all the parameters calculated from the best simulation has a standard error

of 50% or more. This comparison of methods suggests that the synthesis of near-field ground motions is still a great challenge to seismologists.

A credible model of the complex source process is essential for the prediction of ground motion. Although efforts have been made to implement dynamic modeling of extended sources to predict ground motions (Guatteri *et al.*, 2003; Hartzell *et al.*, 2005), high-frequency dynamic fault models are still difficult and computationally expensive. Although the computational limits can be overcome to some degree, these models have been restricted to lower frequencies (less than 2–3 Hz). Kinematic modeling remains the best means of incorporating many aspects of physical models of the earthquake process while still being able to compute broadband strong ground motion (e.g., Hall *et al.*, 1995; Kamae *et al.*, 1998; Pitarka *et al.*, 2000; Hartzell, *et al.*, 2002; Archuleta *et al.*, 2003).

Besides the complications due to the source, complex Earth models significantly influence the amplitude, frequency content, and duration of ground motions. Any accurate ground-motion estimate must include Green's functions that encompass, or try to encompass, the complexity of the velocity structure. In addition, nonlinear site effects are another important issue that should be addressed in ground-motion prediction, because strong ground motions, especially the higher-frequency strong ground motions, can induce nonlinear soil response near the surface.

We present a new method for computing broadband strong ground motions. In our method, the complexity of the source process is represented by spatial distributions of source parameters based on probability distributions. Having the kinematic source model, we use a 3D Earth velocity structure to calculate synthetic ground motions for frequencies up to 1 to 2 Hz. We also compute ground motions to a frequency of 10 to 20 Hz using a layered (1D) Earth model. The exact frequency ranges depend on the frequencies of interest in a particular application and the size and accuracy of the 3D velocity model. Using the 1D synthetics as inputs, we apply a 1D nonlinear wave-propagation code (e.g., Bonilla *et al.*, 1998; Archuleta *et al.*, 2003; Hartzell *et al.*, 2004) to consider local site and soil nonlinear effects near the surface. The 3D ground motions (lower frequencies) and the 1D ground motions (higher frequencies) are stitched together to form the broadband time histories of ground motions. The strong ground motion data set for the 1994 Northridge earthquake is used to validate our prediction method.

Kinematic Modeling by Correlated Random Source Parameters

To model a kinematic faulting process, we divide the fault of the mainshock into subevents. For each subevent we prescribe the slip history. In our kinematic model each subevent is represented by a point source with parameters consisting of the slip amplitude, rake, secant rupture velocity (average rupture velocity between hypocenter and a point on the fault) (Day, 1982), and slip duration (rise time)—all of which are poorly constrained for future earthquakes. To allow for our inadequate *a priori* knowledge we describe these parameters as random variables with constraints on the total seismic moment (magnitude), the high-frequency decay of the spectral amplitudes, the average rupture velocity, and the spatial coherence of source parameters.

In addition, dynamic modeling of a complex rupture process (e.g., Oglesby and Day, 2002; Guatteri *et al.*, 2003) shows that areas of large slip correlate with faster rupture velocity. However, because our model is based on the secant, not the local rupture velocity, we assume that the correlation between secant rupture velocity and slip is about 30%. Larger slip normally requires longer rupture duration. Otherwise the maximum slip velocity could become unreasonably large. We therefore set the correlation between rise time and slip to 60%.

The distribution of rake on the fault is obtained by randomly perturbing an average value of slip rake. In this study we choose the perturbation range of $-40°$ to $40°$ based on a review of previous slip inversions. A flow chart of the entire simulation process is given in Figure 1. The randomly distributed slip amplitudes, secant rupture velocities, and rise times are generated as follows.

Step 1. Three 2D, Gaussian (normal) distributed, white-noise matrices are generated, $\mathbf{N}_1$, $\mathbf{N}_2$, and $\mathbf{N}_3$, with zero mean and unit variance. Each matrix has the same dimensions as the number of point sources along the strike and dip directions of the main fault.

Step 2. Two Gaussian distributed white-noise matrices are derived by

$$\mathbf{N}_2^1 = \eta_1 \mathbf{N}_1 + \sqrt{1 - \eta_1^2}\, \mathbf{N}_2 \quad \text{and} \quad \mathbf{N}_3^1 = \eta_2 \mathbf{N}_1 + \sqrt{1 - \eta_2^2}\, \mathbf{N}_3. \quad (1)$$

Here $\mathbf{N}_2^1$ and $\mathbf{N}_1$ are correlated with a coefficient of η_1, $\mathbf{N}_3^1$ and $\mathbf{N}_1$ are correlated with a coefficient of η_2. The initial values of the two correlation coefficients η_1 and η_2 are set to 0.3 and 0.6, respectively. To enforce a spatial coherence, we apply the spectral representation method in Appendix A to construct three colored (bandpassed) 2D Gaussian random fields, $\mathbf{S}$, $\mathbf{V}$, and $\mathbf{R}$, using the elements of $\mathbf{N}_1$, $\mathbf{N}_2^1$, and $\mathbf{N}_3^1$, respectively, as the required independent Gaussian random variables, and the power spectral density suggested by Mai and Beroza (2002):

$$P(k_x, k_y) = [1 + (k_x C_L)^2 + (k_y C_W)^2]^{-2}, \quad (2)$$

where C_L and C_W are coherence lengths along the strike and dip, respectively. They are calculated using the empirical relations obtained by Mai and Beroza (2002):

$$\log_{10}(C_L) = -2.5 + M_w/2, \quad \text{and} \quad \log_{10}(C_W) = -1.5 + M_w/3. \quad (3)$$

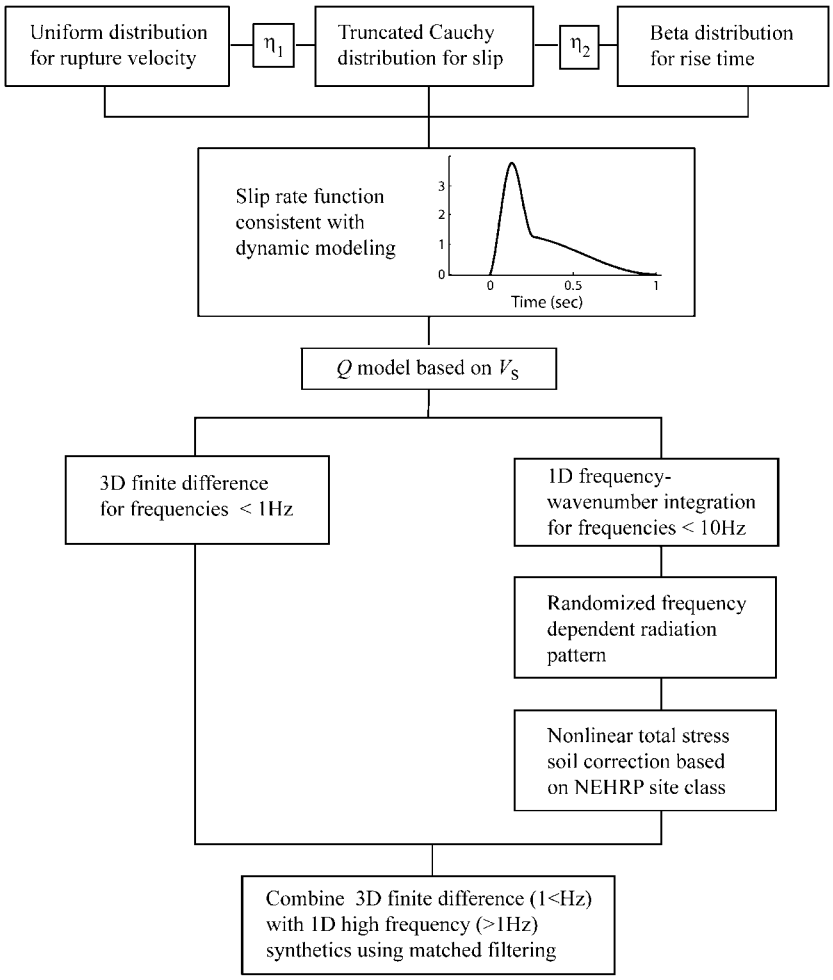

Figure 1. Flow chart of broadband ground-motion simulation method. η_1 and η_2 are spatial correlation coefficients between slip and rupture velocity and between slip and rise time, respectively.

The **S**, **V**, and **R** are stationary Gaussian processes with zero mean. Their mean Fourier amplitude spectra have k^{-2} decay (Herrero and Bernard, 1994; Somerville *et al.*, 1999).

In the following we use the NORmal To Anything (NORTA) method (Cario and Nelson, 1997) to map the three Gaussian random fields, **S**, **V**, and **R**, to the spatial distributions of source parameters that follow our preferable probability distributions. Because we only require that the power spectral densities of the mapped source parameters keep the same shape as those of Gaussian random fields, we can perform the mapping by implementing the basic concept of NORTA, that is, solving the equation:

$$P_S(y) = P_N(x), \tag{4}$$

where x is one component of **S**, **V**, or **R**; P_N is Gaussian probability function; y represents a source parameter that has the probability function P_S.

Step 3. Using the NORTA method (Cario and Nelson, 1997), we map the matrix **S** to slip amplitudes that follow the truncated Cauchy probability distribution:

$$p(D) = C \frac{1}{1 + [(D - D_0)/\kappa)]^2}, \; 0 \le D \le D_{\max}, \tag{5}$$

with the assumptions that the maximum slip of the target event $D_{\max} = 3.5\,\overline{D}$ and $D_0 = 0.5\,\overline{D}$; C is a normalizing factor. Here we chose the Cauchy distribution (Lavallée and Archuleta, 2003; Lavallée *et al.*, 2006) because it allows for larger values of slip amplitude relative to the mean, which is more consistent with previous earthquakes. The value for $D_{\max}$ is based on a consideration of the slip-inversion results for the 1994 Northridge earthquake. The slip distribution is insensitive to D_0, which can have values between 0 and $\overline{D}$. The factor κ is determined in such way that random variables generated from equation (4) have a mean value of $\overline{D}$. In practice we first set $\overline{D} = 1$ and multiply the generated slips by a 2D window to taper the slip to zero at the edges of the fault. Then we multiply the windowed slip amplitudes by a factor to ensure that the synthetic seismic moment is equal to the seismic moment of the target event.

Similarly, we map the matrix **V** to secant rupture velocity and **R** to rise time. A survey of previous earthquakes in California shows they have an average rupture velocity of about 0.8 V_S (Geller, 1976; Somerville *et al.*, 1999). We calculate the secant rupture velocities V_r using a uniform distribution between 0.6 and 1.0 V_S. The rupture velocities generated from this distribution have a mean value of 0.8 V_S, which is an average value for many observed ruptures.

For the rise time we consider a beta distribution:

$$p(\tau) = C\,(\tau - \tau_{\min})(\tau_{\max} - \tau)^2; \quad \tau_{\min} \le \tau \le \tau_{\max}. \quad (6a)$$

The beta distribution is used for rise time because it has fixed upper and lower bounds. We assume $\tau_{\min} = 0.2\,\tau_{\max}$, where $\tau_{\max}$ is determined by matching the spectral levels at high frequency, basically infinity, to the Brune ω^{-2} model (Brune, 1970). Since the slip-rate functions (equations 7a, 7b) that we use for each point source have ω^{-2} decay at very high frequency, the following equation will hold:

$$(Mf_c^2)^2 = \sum_{i=1}^{N}\left(\frac{m_i b}{\tau_i^2}\right)^2, \quad (6b)$$

where M and f_c are moment and corner frequency of the large event, respectively; N is the number of point sources used to simulate the source process of the large event; m_i is the moment of point source i; b is constant factor, which depends on the form of the slip-rate function of the point source; and τ_i is the rise time of point source i. According to equation (6a) we can derive that

$$\tau_i = r_i \tau_{\max}, \quad (6c)$$

in which, the random number r follows

$$f(r) = C\,(r - 0.2)\,(1 - r)^2, \quad 0.2 \le r \le 1. \quad (6d)$$

Combining equations (6b) and (6c) we can determine $\tau_{\max}$.

Step 4. We compute the correlation coefficient between slip and secant rupture velocity, and between slip and rise time. These coefficients may not be equal to the prescribed values of 0.3 and 0.6, respectively, because we have filtered and nonlinearly transformed (mapped) the three white-noise matrices. In this case we choose a new value for η_1 and/or η_2 based on the computed correlation coefficients, and repeat steps 2 to 4 until the computed coefficients fit the prescribed values within a given tolerance. Both Graves and Pitarka (2004) and Hartzell *et al.* (2005) have considered rupture velocities that are linearly related to the slip amplitude, but this article is the first to use correlated random distributions to represent the relationship between slip and rupture velocity and between slip and rise time.

The choice of the functional form of slip rate for a point source (used for each subelement on the fault) is a principal component in the prediction of broadband ground motion. Our selection is motivated by the results of dynamic fault modeling (Guatteri *et al.*, 2004). We construct the slip-rate function (Fig. 2) as

$$\dot{s}(t) = \begin{cases} C_N[0.7 - 0.7\cos(\pi t/\tau_1) + 0.6\sin(0.5\pi t/\tau_1)] & 0 \le \tau < \tau_1 \\ C_N[1.0 - 0.7\cos(\pi t/\tau_1) + 0.3\cos(\pi(t - \tau_1)/\tau_2)] & \tau_1 \le \tau < 2\tau_1, \\ C_N[0.3 + 0.3\cos(\pi(t - \tau_1)/\tau_2)] & 2\tau_1 \le \tau < \tau \end{cases} \quad (7a)$$

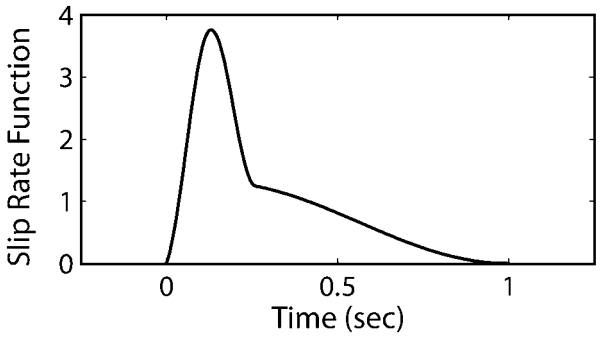

Figure 2. Normalized slip-rate function (equations 7a, 7b) of a point source.

where

$$C_N = \pi / (1.4\pi\tau_1 + 1.2\tau_1 + 0.3\pi\tau_2), \quad (7b)$$

and τ is rise time, $\tau_1 = 0.13\tau$, $\tau_2 = \tau - \tau_1$. Both the first and second derivatives of this slip-rate function have a nonzero value at the starting time. This feature implies that the initial phase of the simulated rupture process will radiate high-frequency energy. Also note (Fig. 2) that the slip-rate function is not symmetric—characteristic of slip-rate functions determined in dynamic simulations (e.g., Andrews, 1976; Day, 1982). Graves and Pitarka (2004) have used a similar nonsymmetric-shaped slip-rate function.

Through consideration of many different slip models, we find that the predicted ground motion is relatively insensitive to the value of maximum slip amplitude ($D_{\max}$), as long as it allows sufficient variance of slip. The rise time needs a distribution that is bounded, so that extreme values are not encountered. However, our results show high sensitivity to the distribution of rupture velocity. Because of the present limited results for observed rupture velocities, we have chosen a simple uniform distribution.

Computing Broadband Ground Motions

We use the single-source model derived in the preceding section to separately compute low- and high-frequency ground motions. After considering the nonlinear site effect, the low- and high-frequency predictions are stitched together to generate the broadband ground motions.

We use a 3D Earth model and the 3D viscoelastic, fourth-order, finite-difference (FD) algorithm of Liu and Archuleta (2002) to calculate synthetic ground motions for frequencies up to 1 to 2 Hz. This FD code uses the perfectly

matched layer method to model an artificial boundary (Collino and Tsogka, 2001; Marcinkovich and Olsen, 2003) and a coarse-grained method to model attenuation (Day and Bradley, 2001; Liu and Archuleta, 2006). This code is fully parallelized, and in addition, it allows for two regions with different grid sizes. The surface region has a factor of 3 finer grid spacing, required by the lower shear-wave velocities. The underlying region, with larger spacing, allows the model to be continued to depth with a much lower memory requirement. The 3D velocity structure incorporates the geometry of the geology in the area, including the deep sedimentary basin structures that can lead to the trapping of seismic energy and production of strong surface waves.

There is difficulty in extending the FD calculations to higher frequencies (>2 Hz) because of our poor knowledge of the subsurface geological medium and the limitation of computational facilities. We use a layered Earth model (1D) and a frequency-wavenumber (FK) code (Zhu and Rivera, 2001) to generate ground motions to higher frequencies (e.g., 10 to 20 Hz). The 1D computations are very efficient for obtaining high-frequency synthetics, but they do not account for scattering effects that can reduce the influence of radiation patterns on high-frequency ground motions and increase the ground-motion duration. This disadvantage can be overcome in part in our 1D computations by randomly perturbing the given strike, dip, and rake angle of faulting. Let φ represent the strike, dip, or rake angle of a point source on the fault plane; we express φ as a frequency-dependent random value (Pitarka *et al.*, 2000; Zeng and Anderson, 2000):

$$\varphi_i = \begin{cases} \varphi_0 & f \le f_1 \\ \varphi_0 + (f - f_1) / f_2 - f_1)((2r_i - 1)\varphi_p, & f_1 < f < f_2, \\ \varphi_0 + (2 * r_i - 1) * \varphi_p & f_2 \le f \end{cases} \quad (8)$$

where φ_0 is the given value of strike, dip, or rake angle of the fault; φ_p is the maximum perturbation that can be added on to φ_0; r_i is a random number uniformly distributed between 0 and 1; the subscript i denotes the index of point sources. The perturbation on φ_0 linearly increases when the frequency f varies from f_1 to f_2. In this study we use $f_1 = 1$ Hz and $f_2 = 3$ Hz, and set φ_p to be 50° for strike, 40° for rake, and 30° for dip. The results are insensitive to these values as long as they allow for sufficient variance.

The local site and soil nonlinear effects are incorporated into the synthetic ground motions by using a 1D nonlinear approach (e.g., Bonilla *et al.*, 1998; Hartzell *et al.*, 2004). To do so, the synthetic ground motion at the surface is first deconvolved using the linear response of the surface layers to a sufficient depth, below which there is no nonlinearity. This deconvolved time history is then nonlinearly propagated back to the surface using the available geotechnical information near the surface. The 3D synthetics over basin structures are likely to contain strong surface waves, which propagate mostly horizontally near the surface. We cannot use this 1D code to compute the nonlinear soil response for surface waves. Therefore, we only apply the 1D nonlinear correction to the 1D synthetics over their entire frequency range. Before combining the 3D and 1D synthetics, we estimate the difference in *S*-wave travel times between the 3D and 1D synthetics using a waveform cross correlation. Based on this estimation we shift the 3D synthetics such that the first *S* waves of the 1D and 3D ground motions arrive at approximately the same time. Finally, we combine the high-frequency components of the 1D ground motions with the low-frequency components of the 3D synthetics to produce a broadband time history of ground motion. The combination of the two synthetics is accomplished using the match-filter technique (Hartzell and Heaton, 1995), where the same filter corner frequency and rolloff characteristics are used to low-pass filter the 3D synthetics and high-pass filter the 1D synthetics.

Validation of the Method

The method is evaluated using the strong-motion data set from the 1994, M_w 6.7, Northridge earthquake. This earthquake is a good event to use because of the complex geology of the Los Angeles area and the large number of near-field ground-motion records. For our prediction experiment, we chose the fault model geometry and hypocenter based on Hartzell *et al.* (1996). The fault strikes 122° and dips 40° to the southwest. The fault plane extends from a depth of 5 to 21 km, with a fault width of 20 km. The hypocenter is located at 34.211° N, 118.546° W and a depth of 17.5 km. The slip rake has an average angle of 105° and the total seismic moment is 1.23×10^{19} N m.

The fault area is first discretized into 128 rectangular elements along strike and 128 elements downdip for a total of 16,384 subfaults (or point sources). The interval between two adjacent point sources is small enough to accurately simulate the rupture directivity effects up to 4 Hz (Spudich and Archuleta, 1987). (For smaller-magnitude events the point source spacing can be reduced to maintain the properties of the randomized source parameters.) The spatial distribution of slip, secant rupture velocity, and rise time are then generated using the method described in the previous section. During this procedure a 1D-velocity model (discussed next) is adopted to calculate the seismic moment and rupture velocity of each point source. The corner frequency of the Northridge earthquake is specified at 0.14 Hz—one over the effective rupture time defined as the shortest fault dimension (20 km) divided by the average rupture velocity (2.8 km/sec). In Figure 3 we plot an example of the spatial distributions of the generated source parameters for the Northridge earthquake. Even though the slip distribution in Figure 3 was randomly generated, it has some similarities with slip distributions obtained from finite-fault inversion studies of this earthquake (Wald *et al.*, 1996; Hartzell *et al.*, 1996). We did not, however, consider multiple slip distri-

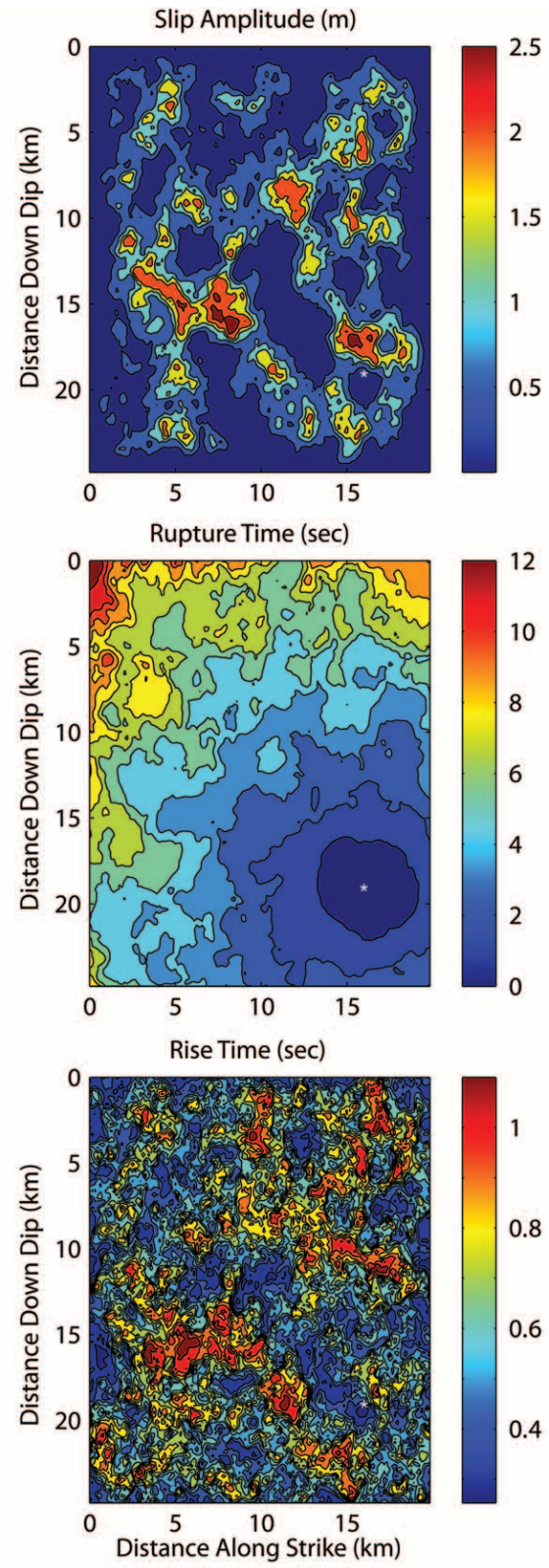

Figure 3. The generated spatial distributions of the slip amplitude, secant rupture velocity, and rise time. The secant rupture velocity (average rupture velocity between hypocenter and a point on the fault) and the rise time are correlated with slip amplitude with a coefficient of 0.3 and 0.6, respectively.

butions because Hartzell *et al.* (2005) had shown that the mean bias and standard deviation of the fit to the strong-motion data is less sensitive to the slip distribution and more sensitive to the distributions of rupture velocity and rise time. We find that the rupture velocities and rise times are positively correlated with slip amplitudes as a result of the application of equations (1)–(6).

The two horizontal components of strong motions recorded at 30 stations (Table 1) are used in this validation. Figure 4 shows the station locations relative to the surface projection of the Northridge fault plane. The site classifications for these stations are also listed in Table 1 (NGA-Flatfile). We use Version 3 of the Southern California Earthquake Center (SCEC) 3D seismic-velocity model (Magistrale *et al.*, 2000) and our 3D FD method to calculate the synthetic ground motions for frequencies up to 1 Hz. In this calculation, the lowest shear-wave velocity is 550 m/sec, requiring a minimum grid interval of 100 m. For attenuation, because the Q-structure is not available in the SCEC Version 3 model, we prescribe Q_s as

$$Q_S = \begin{cases} 0.06V_S & V_S \le 1000 \\ 0.14V_S, & 1000 < V_S < 2000 \\ 0.16V_S & 2000 \le V_S \end{cases} \qquad (9)$$

with $Q_p = 1.5\ Q_s$, where shear-wave velocity V_s has the units of meters per second. This Q-structure is similar to the relationship used by Hartzell *et al.* (2006) to model ground-motion records in the Santa Clara Valley, California.

Hartzell *et al.* (1996) used two layered (1D) Earth models in their finite-fault inversion of the Northridge earthquake (Table 2). We adopt these two models to calculate Green's functions up to 10 Hz using the FK code of Zhu and Rivera (2001). The 1D model for rock sites is used at stations classed as B and BC. The soil site 1D model is used for stations classified as C, CD, and D. The Q-values in the 1D calculations are also determined using equation (9). As aforementioned, the subfault size of the generated source model is suitable for computing synthetic ground motions up to 4 Hz. Therefore, we divide each subfault into a 3×3 finer grid and sum the Green's functions at the nine grid points with appropriate rupture-time delays to obtain the Green's functions for each subfault. Synthetics are computed for every subfault by convolving the Green's functions with the source functions and summing to produce seismograms for the 1D calculations.

We use the Fortran code NOAHW (Bonilla *et al.*, 1998; Hartzell *et al.*, 2004) to compute the nonlinear soil response near the surface after linearly deconvolving the 1D synthetics to a depth of 300 m. In the NOAHW code, the Iwan (1967) model is implemented to take into account soil nonlinearity and the stress–strain relation is specified by a given modulus reduction curve. In this study we adopt the modulus reduction curves of Electric Power Research Institute (EPRI)

Table 1
Strong-Motion Recording Station List

Station Name	Location*	Latitude	Longitude	Site Category
BALD	LA; Baldwin Hills	34.0090	−118.3610	CD
CNPK	Canoga Park	34.2120	−118.6010	D
ECC	Energy Control Center-Ground Flr	34.2590	−118.3360	C
GRIF	Griffith Park Observatory	34.1180	−118.2990	B
HSBF	LA; Hollywood Storage FF	34.0900	−118.3390	CD
JENG	Jensen Filtration Plant-Gen. Bldg. Gnd	34.3120	−118.4960	C
KAGC	Pacoima; Kagel Canyon	34.2880	−118.3750	C
LAWL	LA, 8510 Wonderland Ave.	34.1150	−118.3800	BC
NEWH	Newhall; LA County Fire Station	34.3870	−118.5300	D
NHCC	N Hollywood, Coldwater Canyon	34.1940	−118.4120	C
NORD	Arleta; Nordhoff Fire Station	34.2360	−118.4390	D
NWHP	Newhall, 26835 Pico Canyon Blvd	34.3910	−118.6220	D
PACD	Pacoima Dam-Downstream	34.3340	−118.3960	BC
PARD	Pardee	34.4350	−118.5820	D
RRS	Rinaldi Receiving Station-FF	34.2810	−118.4790	D
RSE	Receiving Station E-Ground Flr.	34.1760	−118.3600	D
SATI	17645 Saticoy St, Northridge	34.2090	−118.5170	D
SCRS	Stone Canyon Reservoir Site	34.1060	−118.4540	C
SMCH	Santa Monica City Hall-Ground Flr.	34.0110	−118.4900	CD
SPVA	Sepulveda VA Hospital-Ground Flr	34.2490	−118.4750	D
SSUS	Santa Susana	34.2310	−118.7130	BC
SVSC	Simi Valley School, 6334 Katherine	34.2640	−118.6660	C
SYLM	Sylmar-Olive View Parking Lot	34.3260	−118.4440	CD
TMPL	LA; Temple and Hope	34.0590	−118.2460	CD
TPFS	Topanga Fire Station	34.0840	−118.5990	CD
UCLG	UCLA; Grounds	34.0680	−118.4390	CD
VERM	LA-3620 S. Vermont Ave.	34.0200	−118.2900	D
VNUY	Van Nuys-Seven-story hotel	34.2210	−118.4710	D
WADS	Wadsworth VA Hospital-South	34.0500	−118.4480	C
WOOD	Wood Ranch Reservoir	34.2400	−118.8200	C

*LA, Los Angelos; Flr, floor; FF, first floor; Gen. Bldg. Gnd, generator building ground; VA, Veterans Administration.

(1993). Nonlinear damping comes from the hysteretic stress–strain loops that follow the Masing criteria (Masing, 1926). Silva *et al.* (1998) developed average shear-wave velocity profiles for NEHRP site categories B, BC, C, D, and E. We have adopted these velocity profiles in this study. We also average the velocity profiles for categories C and D to compute the nonlinear site response at stations classified as CD.

Combining low-frequency components of the 3D synthetics with the high-frequency components of the 1D results, we obtain broadband synthetic ground motions. At present, we choose a crossover frequency at 1 Hz. As our knowledge of 3D velocity structures improves, the crossover frequency can be raised. Comparison of broadband predictions and ground-motion records is made by calculating the bias and the standard error of the predicted ground-motion parameters, such as Fourier amplitude spectra or response spectra. Following the work of Abrahamson *et al.* (1990) and Schneider *et al.* (1993), the bias of predictions is given by

$$B = \frac{1}{N}\sum_{i=1}^{N}\left[\ln(O_i) - \ln(S_i)\right] \tag{10a}$$

and the standard error is estimated by

$$E = \sqrt{\frac{1}{N}\sum_{i=1}^{N}\left[(\ln(O_i) - \ln(S_i)) - B\right]^2}, \tag{10b}$$

where N is the total number of horizontal components of motion, S_i and O_i are the synthetic and observed ground-motion parameters, respectively. Figure 5 plots the bias and standard error versus frequency (or period) for acceleration Fourier spectra and 5% damped response spectra. The average bias of Fourier spectra over 30 stations and both horizontal components is close to zero for the frequency band 0.3 to 10 Hz. The large negative values in bias below 0.3 Hz, which indicates overprediction, are mostly caused by high-pass filtering of the data records. The predicted response spectra have no significant bias over the period range 0.1 to 10 sec. In particular, the response spectrum does not show a large bias at long periods. The small bias at long periods is because response spectral values at these periods are influenced by the amplitudes of shorter-period waves. Because the shorter-period waves have a low bias and larger amplitude, they result in a lower bias at longer periods. The stan-

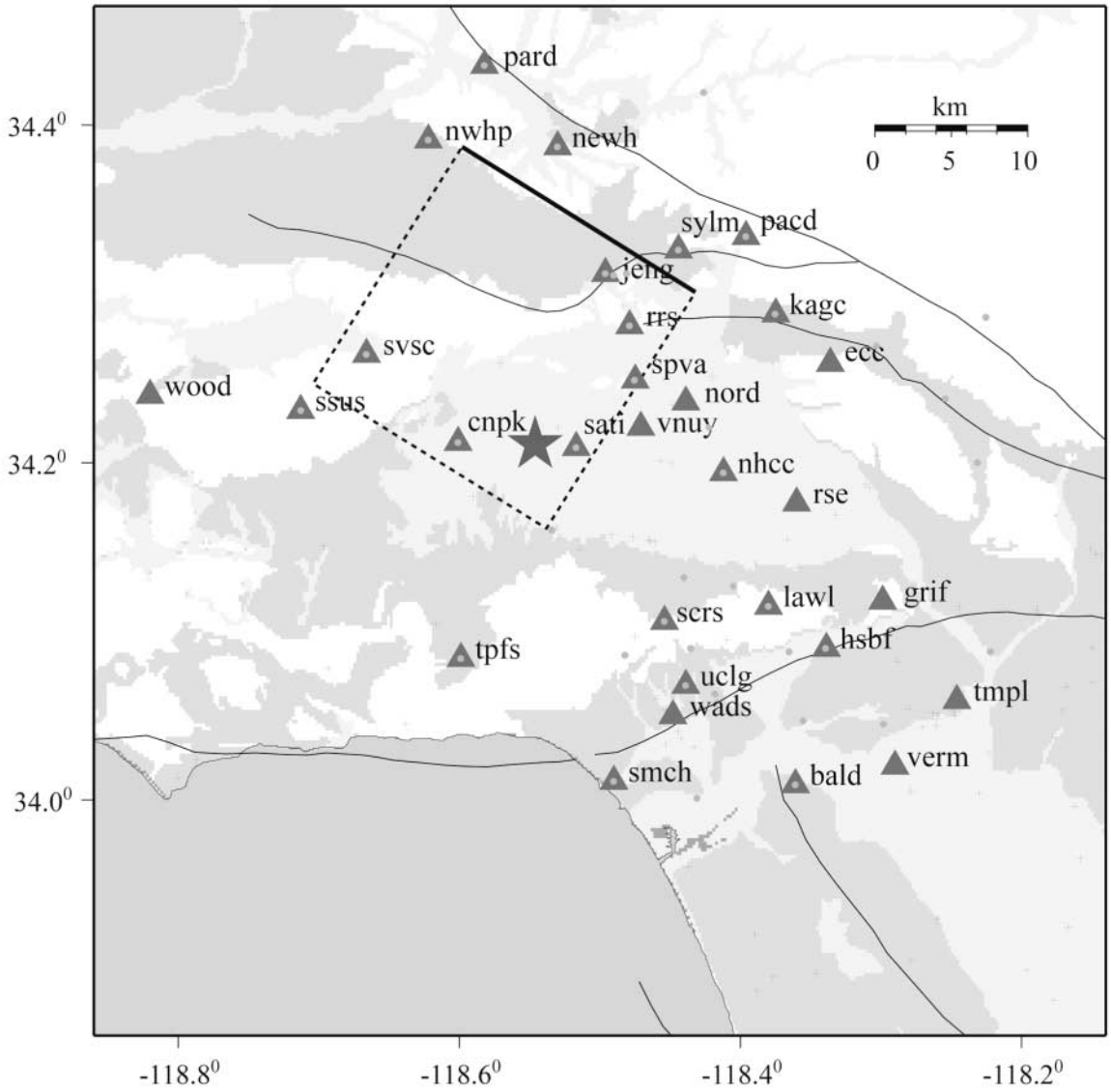

Figure 4. Locations of stations used to validate the prediction method. The box shows the surface projection of the Northridge model fault plane.

dard errors of response spectra are about 0.5 (natural logarithm, Table 3), similar to the best results of other investigators (Graves and Pitarka, 2004; Hartzell *et al.*, 1999, 2005; Zeng, 2006). The synthetics obtained by combining 1D and 3D results have smaller bias and standard error at low frequencies, indicating that using a 3D velocity structure improves the long-period ground-motion predictions.

Figure 6 compares broadband synthetic velocities (0.1 to 10 Hz) in the time domain with observed strong-motion records. Here we show two horizontal components of ground motion, parallel and perpendicular to the fault strike direction. For most stations, both horizontal synthetic and observed velocities have similar strong-motion durations (determined visually) except for station NORD, which shows a large late-arriving waveform in the synthetics. This arrival is generated by the local 3D velocity model because it is not found in the 1D synthetics. Our synthetic time histories also reproduce much of the same character and frequency content versus time seen in the data records. For example, both synthetics and observations have a simple velocity pulse on the fault-perpendicular component at stations NWHP, JENG, and SYLM, located along the top edge of the fault.

Conclusions

The method presented in this study is intended for the prediction of broadband ground-motion time histories from future scenario earthquakes. It uses spatially correlated distributions of randomized source parameters to describe the kinematic source process. We have validated the method by using data from the Northridge earthquake. Our model bias and standard error are similar to the best results obtained

Table 2
Layered Velocity Structure Model

Thickness (km)	V_P (km/sec)	V_S (km/sec)	Density (g/cm^3)	Q_P	Q_S
		Rock Site			
0.5	1.9	1.0	2.1	90	60
1.0	4.0	2.0	2.4	420	280
2.5	4.7	2.7	2.6	567	378
23.0	6.3	3.6	2.8	864	576
13.0	6.8	3.9	2.9	936	624
—	7.8	4.5	3.3	1080	720
		Soil Site			
0.1	1.2	0.3	1.7	27	18
0.2	1.6	0.5	1.8	45	30
0.2	1.9	1.0	2.1	90	60
1.0	4.0	2.0	2.4	420	280
2.5	4.7	2.7	2.6	567	378
23.0	6.3	3.6	2.8	864	576
13.0	6.8	3.9	2.9	936	624
—	7.8	4.5	3.3	1080	720

Table 3
Bias and Standard Error at Selected Frequencies

Frequencies (Hz)	Fourier Spectra		Response Spectra	
	Bias	Standard Error	Bias	Standard Error
0.1	−0.967	1.721	−0.234	0.404
0.5	−0.064	0.511	0.030	0.369
1.0	0.005	0.531	0.031	0.388
3.0	0.100	0.498	−0.006	0.447
5.0	−0.025	0.676	−0.071	0.557
7.0	−0.121	0.595	−0.085	0.506
10.0	−0.152	0.784	−0.061	0.506

from other techniques. In our validation, however, the faulting model used to generate the broadband synthetics is constrained only by general considerations of the earthquake moment, fault dimensions, mechanism, and hypocentral location. In addition, average velocity profiles for each NEHRP site category are used to correct for local site effects and soil nonlinear response.

The variation in ground motions predicted by our method results from both modeling and parametric uncertainties. The standard error estimated from the validation process can be used as a measurement of the modeling uncertainty. The parametric uncertainty consists of the uncertainties in our input parameters: seismic moment, corner frequency of the mainshock, geometry of the main fault (strike, dip, length, and width), and location of the hypocenter. Effects of the uncertainties in these parameters can be considered by performing a suite of predictions for a reasonable range of values for these parameters. Moreover, as we compute a wide range of ground motions for a particular target event, we can also determine where a specific event, such as Northridge, falls within the computed range. Note that both forms of uncertainty can be influenced by the distribution of

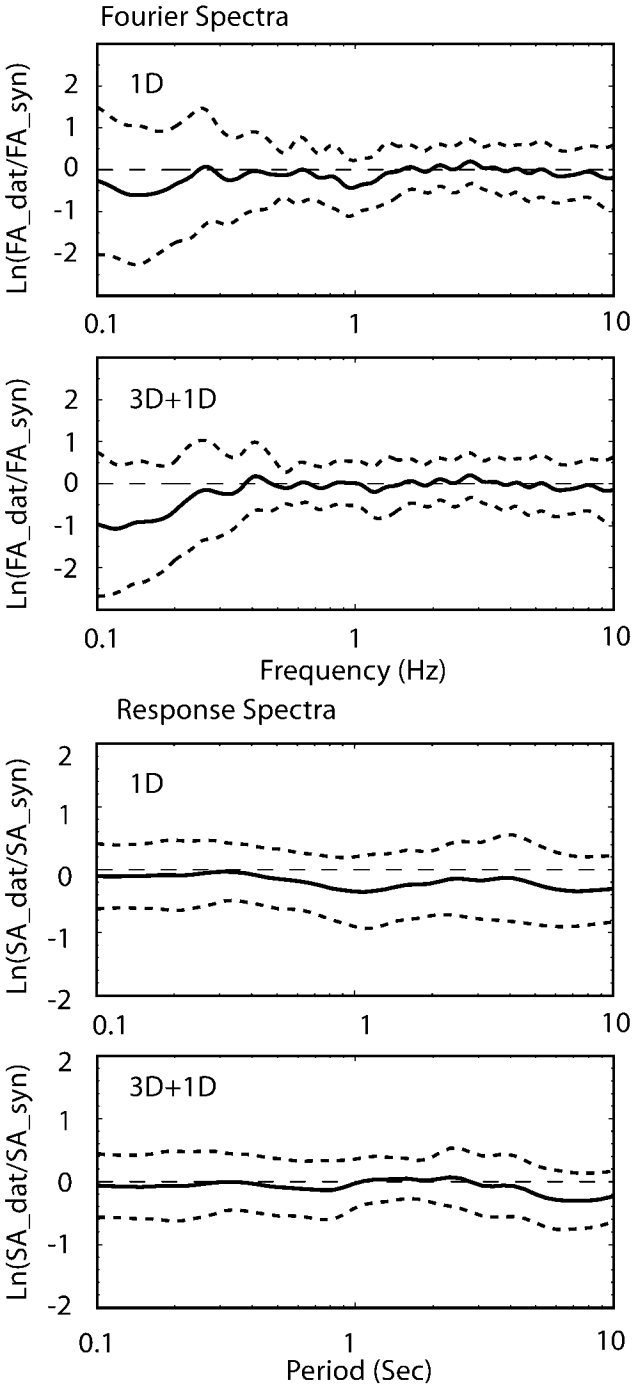

Figure 5. Average bias with standard error (equations 10a, 10b) for our broadband simulations using 30 stations. The black lines are the plots of bias. The black dashed lines are bias ± one standard deviation. (Top) Fourier amplitude; (bottom) response spectrum. 1D refers to results from a purely 1D model; 1D + 3D are for a hybrid model with frequencies <1 Hz from a 3D calculation and frequencies > 1 Hz from a 1D calculation.

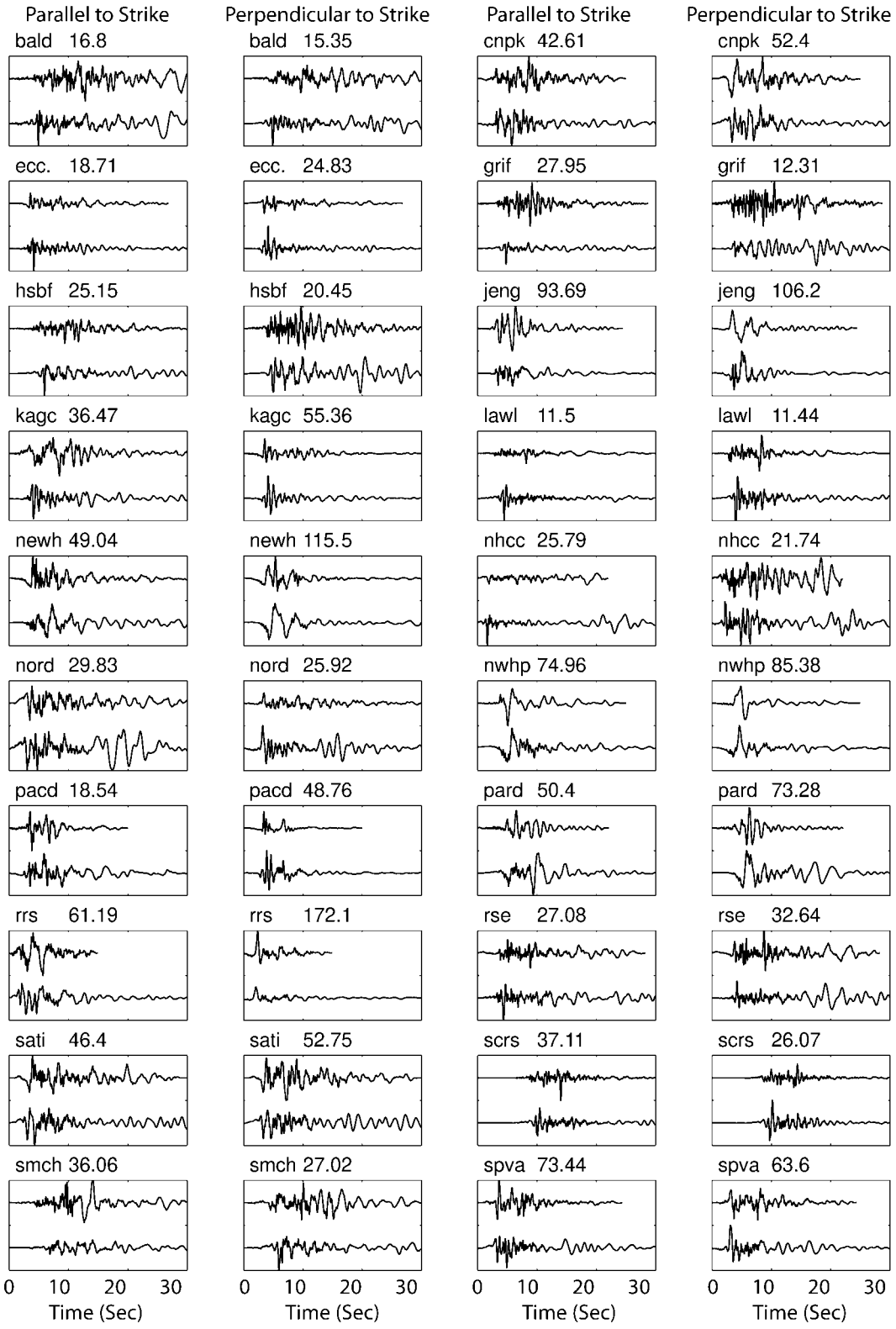

Figure 6. (*caption on next page*)

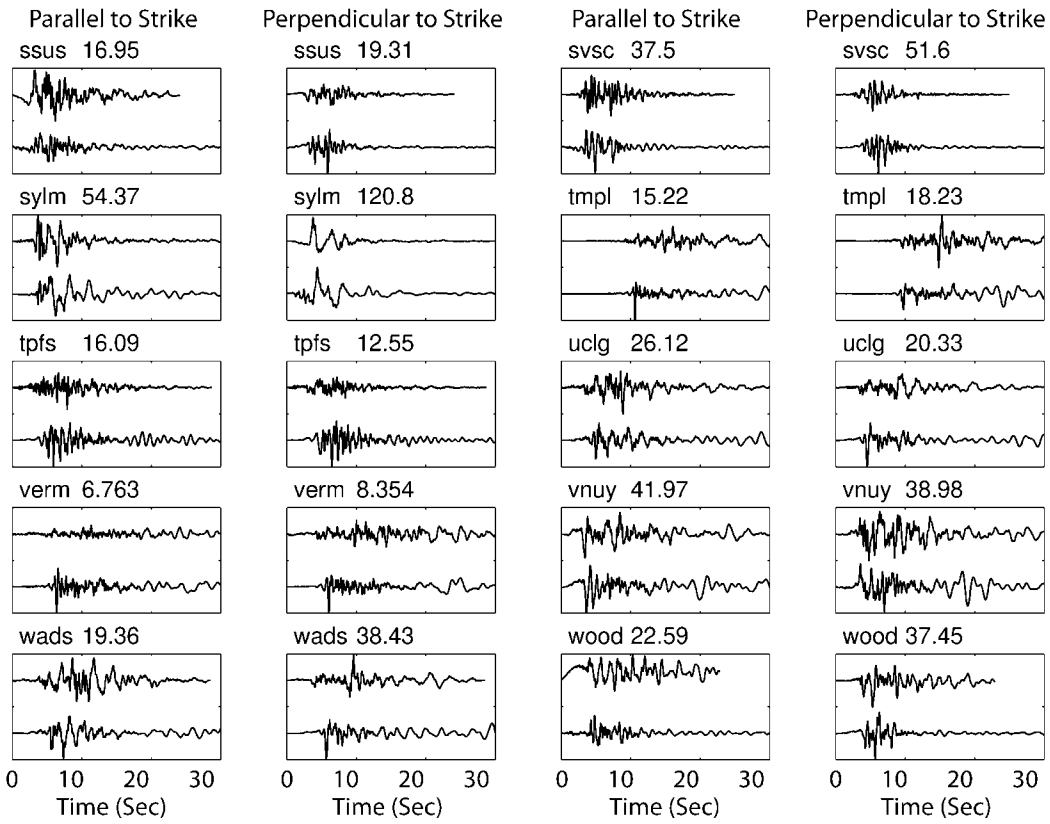

Figure 6. Comparison of the observed and predicted ground velocity waveforms bandpass filtered from 0.1 to 10 Hz. Within each box the observation (top trace) and the synthetics (bottom trace) are plotted with the same vertical scale. The station name is indicated at the top left of the box, followed by peak velocity (centimeters per second) of observation.

observed ground-motion records, with near-field sites being more sensitive to both the stochastic and parametric aspects of the problem. The strengths of our methodology lie in the correlated randomized source parameters that can be used to mimic the results of dynamic modeling and our current knowledge of actual earthquake ruptures, and in the realistic site-response correction that utilizes a nonlinear soil calculation.

Acknowledgments

This article benefited from discussions with Daniel Lavallée and Yuehua Zeng. The records of the Northridge earthquake and the postscript document of Figure 4 were provided by Robert Graves. The 3D calculations were run at the HPC cluster of the High Performance Computing and Communications Center, University of Southern California. We thank R. Graves and G.-Q. Wang for their thoughtful reviews. This work was supported, in part, by National Science Foundation Grant EAR-0122464 (SCEC Community Modeling Environment Project). The 1D calculations were run at the CNSI Computer Facilities, UCSB, sponsored by Hewlett-Packard. The research was funded by the USGS Contract no. 04HQGR0059 and by the Southern California Earthquake Center. SCEC is funded by NSF Cooperative Agreement EAR-0106924 and USGS Cooperative Agreement 02HQAG0008. This is SCEC contribution no. 1034 and ICS contribution no. 0792.

References

Abrahamson, N., P. Somerville, and C. Cornell (1990). Uncertainty in numerical strong motion predictions, in *Proc. of the Fourth U.S. National Conference on Earthquake Engineering*, Vol. 1, 407–416.

Andrews, D. (1976). Rupture propagation with finite stress in antiplane strain, *J. Geophys. Res.* **81,** 3575–3582.

Archuleta, R. J., P-C Liu, J. H. Steidl, L. F. Bonilla, D. Lavallée, and F. Heuze (2003). Finite-fault site-specific acceleration time histories that include nonlinear soil response, *Phys. Earth Planet. Interiors* **137,** 153–181, doi 10.1016/S0031-9201(03)00013-X.

Bonilla, L., D. Lavallée, and R. Archuleta (1998). Nonlinear site response: Laboratory modeling as a constraint for modeling accelerograms, in *Proc. The Effects of Surface Geology on Seismic Motion*, Yokohama, Japan, Vol. 2, 793–800.

Brune, J. N. (1970). Tectonic stress and the spectra of seismic shear waves from earthquakes, *J. Geophys. Res.* **76,** 5002.

Cario, M. C., and B. L. Nelson (1997). Modeling and generation random vectors with arbitrary marginal distributions and correlation matrix, Technical Report, Department of Industrial Engineering and Management Sciences, Northwestern University, Evanston, Illinois.

Collino, R., and C. Tsogka (2001). Application of the PML absorbing layer model to the linear elastodynamic problem in anisotropic heterogeneous media, *Geophysics* **66,** 294–307.

Day, S. M. (1982). Three-dimensional simulation of spontaneous rupture: the effect of nonuniform prestress, *Bull. Seism. Soc. Am.* **72,** 1881–1902.

Day, S. M., and C. R. Bradley (2001). Memory efficient simulation of anelastic wave propagation, *Bull. Seism. Soc. Am.* **91,** 520–531.

Electric Power Research Institute (EERI) (1993). Guidelines for determine design basis ground motions, Electric Power Research Institute Technique Report EPRI TR-102293.

Field, E. H., H. A. Seligson, N. Gupta, V. Gupta, T. H. Jordan, and K. W. Campbell (2005). Loss estimates for a Puente Hills blind-thrust earthquake in Los Angeles, California, *Earthquake Spectra* **21,** 329–338.

Geller, R. J. (1976). Scaling relations for earthquake source parameters and magnitudes, *Bull. Seism. Soc. Am.* **66,** 1501–1523.

Graves, R., and A. Pitarka (2004). Broadband time history simulation using a hybrid approach, in *13th World Conference on Earthquake Engineering*, Vancouver, British Columbia, 1–6 August 2004.

Guatteri, M., P. Mai, and G. Beroza (2004). A pseudo-dynamic approximation to dynamic rupture models for strong ground motion prediction, *Bull. Seism. Soc. Am.* **94,** 2051–2063.

Guatteri, M., P. Mai, G. Beroza, and J. Boatwright (2003). Strong ground-motion prediction from stochastic-dynamic source models, *Bull. Seism. Soc. Am.* **93,** 301–313.

Hall, J., T. Heaton, M. Halling, and D. Wald (1995). Near-source ground motion and its effects on flexible buildings, *Earthquake Spectra* **11,** 569–605.

Hartzell, S., and H. Heaton (1995). San Andreas deterministic fault problem: Green's function summation for a finite source, in *Proceedings: Modeling Earthquake Ground Motion at Close Distances*, EPRI TR-104975, 7-1–7-21.

Hartzell, S., L. F. Bonilla, and R. A. Williams (2004). Prediction of nonlinear soil effects, *Bull. Seism. Soc. Am.* **94,** 1609–1629.

Hartzell, S., S. Harmsen, A. Frankel, and S. Larsen (1999). Calculation of broadband time histories of ground motion: comparison of methods and validation using strong-ground motion from the 1994 Northridge earthquake, *Bull. Seism. Soc. Am.* **89,** 1484–1504.

Hartzell, S., S. Harmsen, R. A. Williams, D. Carver, A. Frankel, G. Choy, P.-C. Liu, R. C. Jachens, T. M. Brocher, and C. M. Wentworth (2006). Modeling and validation of a 3D velocity structure for the Santa Clara Valley, California, for seismic wave simulations, *Bull. Seism. Soc. Am.* **96,** 1851–1881.

Hartzell, S., A. Leeds, A. Frankel, R. Williams, J. Odum, W. Stephenson, and W. Silva (2002). Simulation of broadband ground motion including nonlinear soil effects for a magnitude 6.5 earthquake on the Seattle fault, Seattle, Washington, *Bull. Seism. Soc. Am.* **92,** 831–853.

Hartzell, S., P-C Liu, and C. Mendoza (1996). The 1994 Northridge, California, earthquake: investigation of rupture velocity, rise time and high-frequency radiation, *J. Geophys. Res.* **101,** 20,091–20,108.

Hartzell, S., G. Mariagiovanna, P. M. Mai, P-C Liu, and M. Fisk (2005). Calculation of broadband time histories of ground motion, Part II: Kinematic and dynamic modeling using theoretical Green's functions and comparison with the 1994 Northridge earthquake, *Bull. Seism. Soc. Am.* **95,** 614–645.

Herrero, A., and P. Bernard (1994). A kinematic self-similar rupture process for earthquakes, *Bull. Seism. Soc. Am.* **84,** 1216–1228.

Iwan, W. D. (1967). On a class of models for the yielding behavior of continuous and composite systems, *J. Appl. Mech.* **34,** 612–617.

Kamae, K., K. Irikura, and A. Pitarka (1998). A technique for simulating strong ground motions from great earthquakes, *Bull. Seism. Soc. Am.* **88,** 357–367.

Lavallée, D., and R. Archuleta (2003). Stochastic modeling of slip spatial complexities for the 1979 Imperial Valley, California, earthquake, *Geophys. Res. Lett.* **30,** 1245, doi 10.1029/2002GL015839.

Lavallée, D., P. Liu, and R. J. Archuleta (2006). Stochastic model of heterogeneity in earthquake slip spatial distributions, *Geophys. J. Int.* **165,** 622–640.

Liu, P-C, and R. J. Archuleta (2002). The effect of a low-velocity surface layer on simulated ground motion, *Seism. Res. Lett.* **73,** 267.

Liu, P-C, and R. J. Archuleta (2006). Efficient modeling of *Q* for 3D numerical simulation of wave propagation, *Bull. Seism. Soc. Am.* (in press).

Magistrale, H., S. Day, R. W. Clayton, and R. Graves (2000). The SCEC southern California reference three-dimensional seismic velocity model Version 2, *Bull. Seism. Soc. Am.* **90,** S65–S76.

Mai, P. M., and G. C. Beroza (2002). A spatial random field model to characterize complexity in earthquake slip, *J. Geophys. Res.* **107,** 1–21.

Marcinkovich, C., and K. Olsen (2003). On the implementation of perfectly matched layers in a three-dimensional fourth-order velocity-stress finite difference scheme, *J. Geophys. Res.* **108,** doi 10.1029/2002JB002235.

Masing, G. (1926). Eigenspannungen and verfestigung beim messing, in *Proceeding of 2nd International Congress of Applied Mechanics*, Zurich, Switzerland, 332–335.

Oglesby, D. D., and S. M. Day (2002) Stochastic faulting stress: implications for fault dynamics and ground motion, *Bull. Seism. Soc. Am.* **92,** 3006–3021.

Ogorodnikov, V. A., and S. M. Prigarin (1996). *Numerical Modeling of Random Processes and Fields: Algorithms and Applications*, VSP, Utrecht, the Netherlands.

Pitarka, A., P. Somerville, Y. Fukushima, T. Uetake, and K. Irikura (2000). Simulation of near-fault ground-motion using hybrid Green's functions, *Bull. Seism. Soc. Am.* **90,** 566–586.

Schneider, J., W. Silva, and C. Stark (1993). Ground motion model for the 1989 M 6.9 Loma Prieta earthquake including effects of source, path, and site, *Earthquake Spectra* **9,** 251–287.

Shaw, J., A. Plesch, J. Dolan, T. Pratt, and P. Fiore (2002). Puente Hills blind-thrust system, Los Angeles, California, *Bull. Seism. Soc. Am.* **92,** 2946–2960.

Silva, W., R. Darragh, and N. Gregor (1998). Reassessment of site coefficients and near-fault factors for building code provisions, Pacific Engineering and Analysis Report 98-HQ-GR-1010.

Somerville, P., K. Irikura, R. Graves, S. Sawada, D. Wald, N. Abrahamson, Y. Iwasaki, N. Smith, and A. Kowada (1999). Characterizing crustal earthquake slip models for the prediction of strong ground motion, *Seism. Res. Lett.* **70,** 59–80.

Spudich, P., and R. J. Archuleta (1987). Techniques for earthquake ground-motion calculation with applications to source parameterization of finite faults, in *Seismic Strong Motion Synthetics*, B. A. Bolt (Editor), Academic Press, San Diego, California, 205–265.

Wald, D. J., T. H. Heaton, and K. W. Hudnat (1996). The slip history of the 1994 Northridge, California, earthquake from strong-motion, teleseismic, GPS, and leveling data, *Bull. Seism. Soc. Am.* **86,** S49–S70.

Zeng, Y. (2006). Broadband strong ground motion simulation using a composite source model, *Proceedings of the 8th U.S. National Conference on Earthquake Engineering*, April 18–22, 2006, San Francisco, California, paper no. 1445.

Zeng, Y., and J. Anderson (2000). Earthquake source and near-field directivity modeling of several large earthquakes, in *EERI Proceedings for the Sixth International Conference on Seismic Zonation.*

Zhu, L., and L. Rivera (2001). Computation of dynamic and static displacement from a point source in multi-layered media, *Geophys. J Int.* **148,** 619–627.

Appendix A

Construction of 2D Gaussian Random Fields

We use the spectral representation algorithm described by Ogorodnikov and Prigarin (1996) to generate the 2D Gaussian random fields with given power spectral density (PSD). The primary function of the algorithm is to construct the randomized Fourier spectrum of the random fields. Having the Fourier spectrum, the random field in the spatial domain is obtained by inverse Fourier transformation.

Suppose that a 2D real random field $f(x,y)$ has M sample points with even interval Δx in the X direction, N sample points with even interval Δy in the Y direction, and power spectral density $p(u,v)$. According to the method of Ogorodnikov and Prigarin (1996), the discrete Fourier spectrum of $f(x,y)$ can be expressed as:

$$F(u_k, v_l) = \left[\frac{p(u_k, v_l)}{2}\right]^{1/2} (\xi_{k,l} + i\lambda_{k,l}) \tag{A1}$$

in which, $\xi_{k,l}$ and $\lambda_{k,l}$ are independent Gaussian random variables with zero mean and unit variance; u and v are wavenumbers associated with X and Y directions, respectively; and

$$u_k = \frac{k}{M\Delta x}, \quad k = -\frac{M}{2} + 1,\ldots, \frac{M}{2}; \quad \text{and}$$
$$v_l = \frac{l}{N\Delta y}, \; l = -\frac{N}{2} + 1,\ldots, \frac{N}{2}. \tag{A2}$$

Because $f(x,y)$ is a real function, its Fourier spectrum is symmetric:

$$F(u_k, v_l) = \begin{cases} [F(-u_k, -v_l)]^*, & \text{for any } k \text{ and } l; \\ [F(u_k, -v_l)]^*, & \text{when } k = \dfrac{M}{2}; \\ [F(-u_k, v_l)]^*, & \text{when } l = \dfrac{N}{2}. \end{cases} \tag{A3}$$

Here, the * denotes complex conjugate. In additional, $F(u_k, v_l)$ should be a real variable when the subscripts (k, l) equal (0, 0), (0, N/2), (M/2, 0), or (M/2, N/2). At these four points, $F(u_k, v_l)$ is calculated by

$$F(u_k, v_l) = [p(u_k, v_l)]^{1/2} \xi_{k,l}. \tag{A4}$$

Equation (A1) is applied to compute spectra at points (u_k, v_l), where

$$k = 1,\ldots, \frac{M}{2} - 1, \quad \text{and } l = -\frac{N}{2} + 1,\ldots, \frac{N}{2}; \text{ plus}$$
$$k = 0, \frac{M}{2}, \quad \text{and } l = 1,\ldots, \frac{N}{2} - 1. \tag{A5}$$

Equation (A3) is then used to obtain the spectral values at symmetric points required by the inverse Fourier transform. In the preceding above process of constructing the randomized Fourier spectrum, we need a total of $M \times N$ independent Gaussian random variables.

Institute for Crustal Studies
University of California
Santa Barbara, California 93106
(P.L., R.J.A.)

Department of Earth Science
University of California
Santa Barbara, California 93106
(R.J.A.)

U.S. Geological Survey
Denver Federal Center, Box 25046 MS 966
Denver, Colorado 80225
(S.H.H.)

Manuscript received 17 February 2006.